Electronic Supplementary Material (ESI) for Chemical Science.

Supporting Information for

A High-Spin Square-Planar Fe(II) Complex Stabilized by a Trianionic Pincer-Type Ligand and Conclusive Evidence for Retention of Geometry and Spin State in Solution

Matias E. Pascualini, Natali V. Di Russo, Annaliese E. Thuijs, Andrew Ozarowski, Sebastian A. Stoian, Khalil A. Abboud, George Christou, and Adam S. Veige *
University of Florida, Department of Chemistry, Center for Catalysis, P.O. Box 117200, Gainesville, FL, 32611.

Table of Contents

1. General Considerations.

Unless specified otherwise, all manipulations were performed under an inert atmosphere using standard Schlenk or glovebox techniques. Glassware was oven dried before use. Pentane, tetrahydrofuran (THF), diethyl ether (Et_2O) were dried using a GlassContours drying column. Benzene-d_6 (Cambridge Isotopes) was dried over sodium-benzophenone ketyl and distilled or vacuum transferred and stored over 4Å molecular sieves. Elemental analyses were performed at Complete Analysis Laboratory Inc., Parsippany, New Jersey.

NMR spectra were obtained on Varian Mercury Broad Band 300 MHz, or Varian Mercury 300 MHz spectrometers. Chemical shifts are reported in δ (ppm). For ^{1}H NMR spectra the solvent resonance was referenced as an internal reference.

Variable-temperature dc magnetic susceptibility data was collected in the 5.0 – 300.0 K range using a Quantum Design MPMS-XL SQUID magnetometer equipped with a 7 T dc magnet in an applied field of 0.1 T. The microcrystalline samples were restrained in eicosane to prevent torquing. Diamagnetic corrections using Pascal's constants were applied to the observed susceptibilities to obtain the molar paramagnetic susceptibility (χ_M).

High-frequency EPR spectra were recorded using a home-built spectrometer at the EMR facility of NHMFL. The instrument is a transmission-type device in which waves are propagated in cylindrical lightpipes. The microwaves were generated by a phase-locked oscillator (Virginia Diodes) operating at a frequency of 13 ± 1 GHz and generating its harmonics, of which the 4th, 8th, 16th, 24th and 32nd were available. A superconducting magnet (Oxford Instruments) capable of reaching a field of 17 T was employed.

Mössbauer spectra were recorded using an instrument fitted with a helium-flow Janis 8DT Super Varitemp cryostat that had a built in 8 T, American Magnetics superconducting magnet. The spectrometer was operated in a constant acceleration mode and used a 100 mCi ^{57}Co(Rh) source. This spectrometer allowed for recording variable-temperature spectra from 4.2 to 250 K in applied fields parallel to the incident γ-radiation from 0 to 8 T. All samples consisted of 20-100 mg either amorphous or microcrystalline powders enclosed in custom made Teflon® or Delrin® containers. The containers were loaded under an inert atmosphere in Gainesville and transported to Tallahassee either at 77 K using a standard shipping dewar or at RT in sealed glass vials. Although the cross-section of the Teflon® containers was optimized for recording the high-field EPR spectra, their use with our current Mössbauer setup allowed us to investigate the same sample both by high-field EPR and zero- and low-field Mössbauer spectroscopy. This procedure allowed us to asses both the purity of the EPR samples as well as their field-dependent Mössbauer behavior. The isomer shifts values are quoted against the room-temperature spectrum of a standard Fe metal foil. The spectral simulations were performed using the WMOSS software (SEE Co. formerly WEB Research Co., Edina, MN) and relied on the use of the standard spin-Hamiltonian formalism.

2. Synthesis of 2.

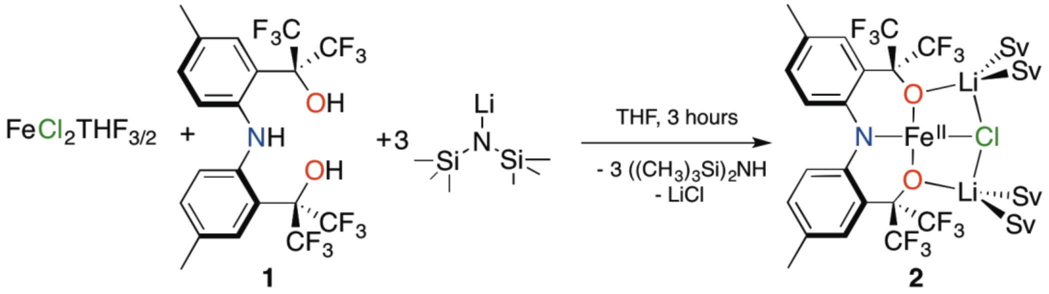

$[CF_3\text{-ONO}]H_3$ (1.000 g, 1.889 mmol) was dissolved in THF (2 mL) and three equivalents of $((CH_3)_3Si)_2NLi$, 97 % (0.978 g, 5.669 mmol) in THF (2 mL) were added drop wise to generate the trianionic $[CF_3\text{-ONO}]^{3-}$ species *in situ*. This solution was slowly added to a THF (2 mL) solution of $FeCl_2THF_{3/2}$ (0.444 g, 1.890 mmol) producing a brown solution. This solution was stirred for 3 h and all volatiles were removed under vacuum. The brown residue was triturated with pentane three times (6 mL), dried under vacuum, and washed with pentane (10 mL). The residue was extracted with diethyl ether (5 mL), filtered through celite and dried under vacuum producing an analytically pure brown microcrystalline powder in 43.6 % yield. Evans method: $\mu_{eff} = 4.91\ \mu_B$. ^{1}H-NMR (C_6D_6, 300 MHz, 25 °C) δ (ppm): 40.05 ($\nu_{1/2}$ = 450 Hz), 34.49 ($\nu_{1/2}$ = 750 Hz), 3.07 ($\nu_{1/2}$ = 300 Hz), 0.66 ($\nu_{1/2}$ = 300 Hz), -1.48 ($\nu_{1/2}$ = 1800 Hz), -2.06 ($\nu_{1/2}$ = 750 Hz), and -24.18 ($\nu_{1/2}$ = 1050 Hz). Elemental analysis calcd. (%) for $C_{36}H_{44}ClF_{12}FeLi_2NO_6$ (919.90 g/mol): C 47.00, H 4.82, and N 1.52; found: C 46.72, H 4.59, and N 1.68.

Red crystals were grown cooling a saturated diethyl ether solution of **2** to -35°C. Evans method: $\mu_{eff} = 5.00\ \mu_B$. ^{1}H-NMR (C_6D_6, 300 MHz, 25 °C) δ (ppm): 37.98 ($\nu_{1/2}$ = 600 Hz), 32.04 ($\nu_{1/2}$ = 1050 Hz), 28.74 ($\nu_{1/2}$ = 1650 Hz), 2.83 ($\nu_{1/2}$ = 300 Hz), 0.41 ($\nu_{1/2}$ = 330 Hz), -3.44 ($\nu_{1/2}$ = 450 Hz), -6.03 ($\nu_{1/2}$ = 1800 Hz), and -25.14 ($\nu_{1/2}$ = 900 Hz). Elemental analysis calcd. (%) for $C_{36}H_{44}ClF_{12}FeLi_2NO_6$ (919.90 g/mol): C 47.00, H 4.82, and N 1.52; found: C 46.92, H 4.65, and N 1.61.

3. ^{1}H-NMR spectroscopy of 2.

The ^{1}H-NMR spectra of brown powder **2** and the red crystals were collected in C_6D_6 and depict paramagnetically broadened signals in the 40 to -25 ppm range. Figure S1 and Figure S2 below show the assignment of the resonances. The π-symmetric magnetic orbitals of Fe^{II} produce a contact shift by a π-delocalization mechanism into the aromatic ring yielding a positive spin density into the C *ortho* and *para* p_z orbitals. This positive spin density causes a negative spin density at the *ortho* H adjacent to it by a spin polarization mechanism. Figure S3 depicts the different mechanisms that lead to the different isotropic shifts in the paramagnetic ^{1}H-NMR. The methyl group located in the *para* position can undergo direct π-delocalization yielding a positive spin density at the H. Therefore, H *ortho* shifts upfield and the Me group protons in *para* shift downfield. The opposite effect, but smaller in magnitude, is observed at the *meta* positions: a negative spin density into the C *meta* p_z orbital causes a positive spin density at the H *meta* which gets shifted downfield. Finally, the remaining signals correspond to THF and Et_2O.

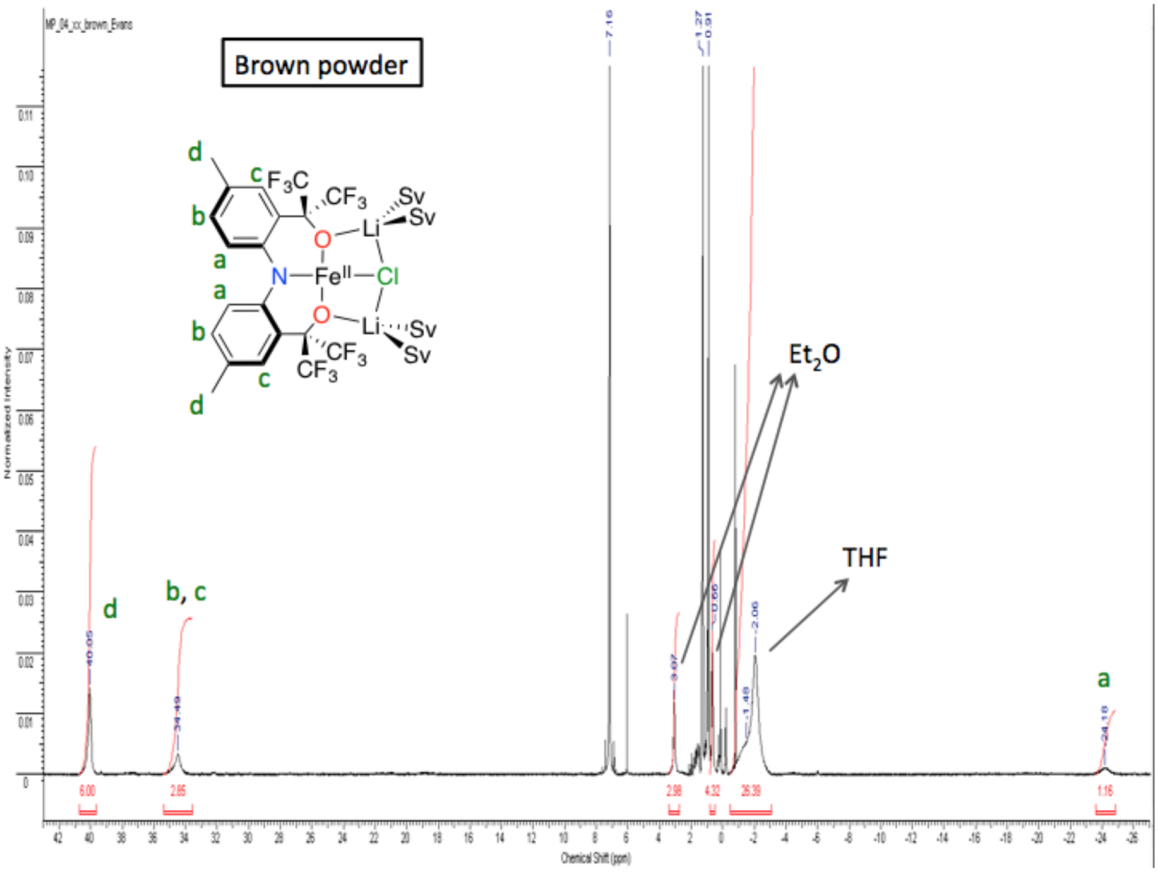

Figure S1. ^{1}H NMR spectrum of **2** in C_6D_6.

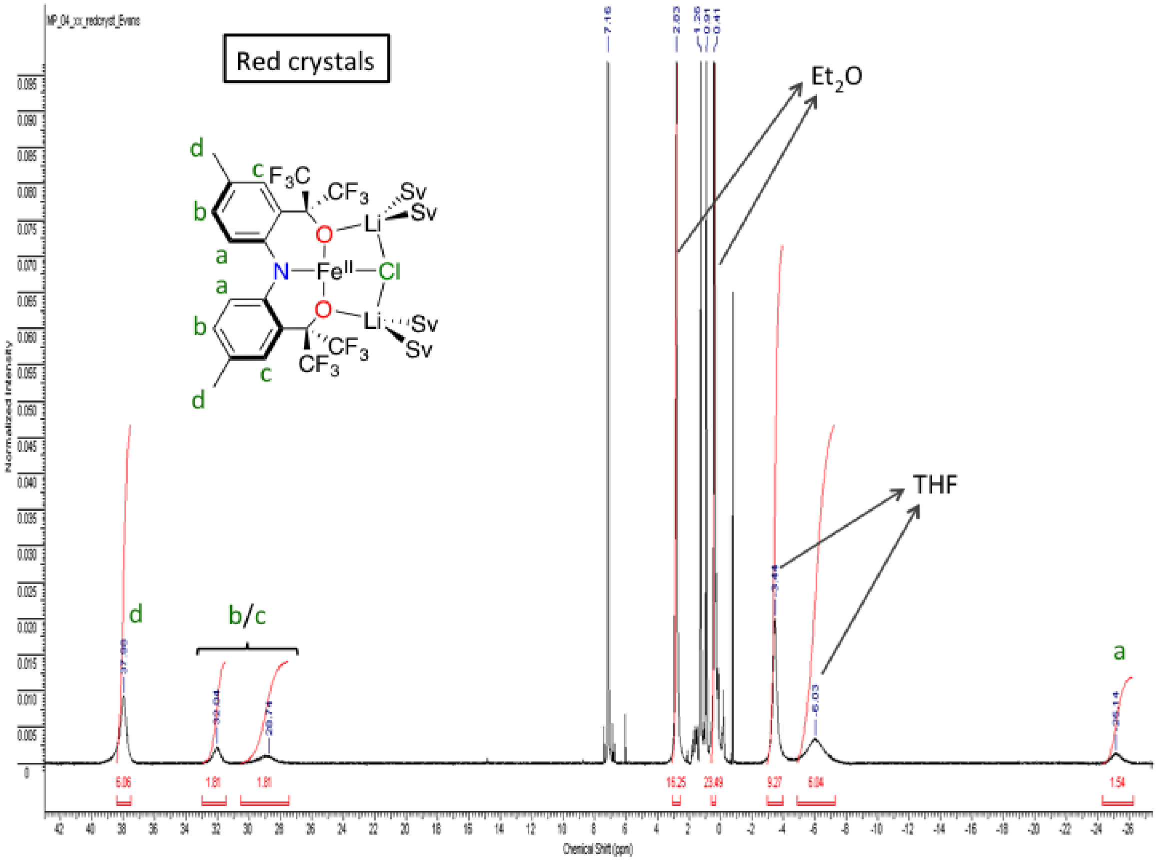

Figure S2. ^{1}H NMR spectrum of red crystals in C_6D_6.

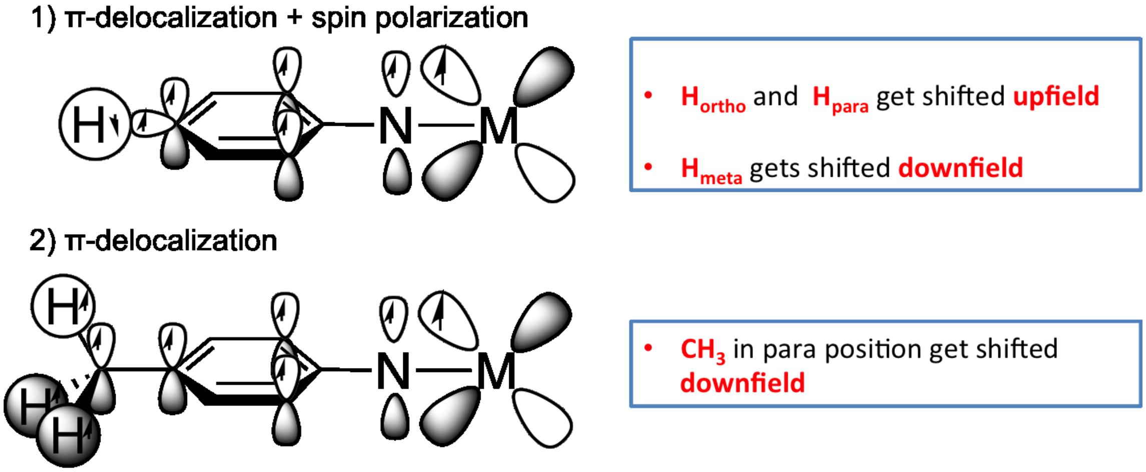

- H_{ortho} and H_{para} get shifted **upfield**
- H_{meta} gets shifted **downfield**

- CH_3 in para position get shifted **downfield**

Figure S3. π-delocalization and spin polarization mechanisms, and their effect in paramagnetic ^{1}H-NMR.

Red crystals of **2** were dissolved in C_6D_6 and titrated with THF in increments of 0.5 equivalents. A ^{1}H-NMR spectrum was collected for **2** and after every THF addition as shown in Figure S4. After the addition of approximately 1 eq of THF, the ^{1}H-NMR spectrum of the red crystals cleanly transforms into the one of **2**. The addition of a second equivalent of THF produces further changes in the chemical shifts. The addition of more than 2 equivalents of THF only sharpens the resonances, but does not change the position of the peaks.

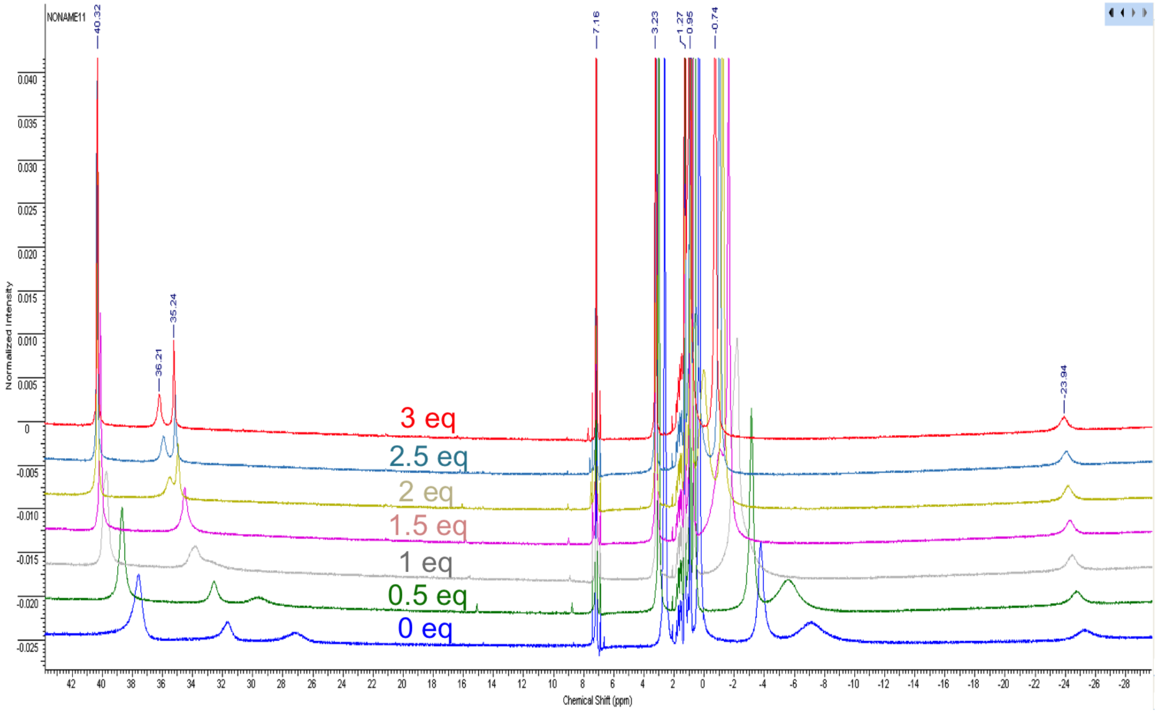

Figure S4. Titration of red crystals of **2** with THF in C_6D_6 followed by ^{1}H-NMR.

4. SQUID magnetometry of 2.

Figure S5 depicts the plot of $\chi_M T$ vs T for complex **2**. $\chi_M T$ steadily decreases with decreasing temperature from 3.16 cm^3 mol^{-1} K at 300 K to 1.25 cm^3 mol^{-1} K at 5.0 K. The 300 K value is higher than the expected spin-only (g = 2) value of 3.00 cm^3 mol^{-1} K for a high spin Fe^{II} complex, which can be attributed to the presence of significant spin-orbit coupling effects. It has been previously seen that high spin Fe^{II} square planar complexes possess an appreciable zero-field splitting (ZFS) parameter, *D*. On the basis of this consideration, the experimental magnetic susceptibility data were fit to the theoretical expression given in eq. S1, which describes the powder average χ_M vs T behavior for an *S* = 2 ion undergoing zero-field splitting, where x = *D/kT, N* is Avogadro's number, *D* is the axial single-ion ZFS parameter, TIP is the temperature-independent paramagnetism, Θ is the Weiss constant, and *g* is the average *g* factor.

$$\chi_M = \frac{Ng^2\mu_\beta^2}{3k(T-\theta)}\left[\frac{2e^{-x}+8e^{-4x}}{1+2e^{-x}+2e^{-4x}}\right] + \frac{2Ng^2\mu_\beta^2}{3k(T-\theta)}\left[\frac{\frac{6}{x}(1-e^{-x})+\frac{4}{3x}(e^{-x}-e^{-4x})}{1+2e^{-x}+2e^{-4x}}\right] + \text{TIP} \quad \text{(eq. S1)}$$

The data were fit in the temperature range of 300 K – 5 K, and yielded fit parameters of $|D|$ = 20.9(4) cm^{-1}, g = 2.05(3), Θ = 0.8 K, and no TIP term. The Weiss constant can be determined from a plot of 1/χ_M vs T. The value obtained from this plot was in good agreement with the value obtained from the fit, suggesting the presence of intramolecular exchange interactions. As has been noted in other studies, powder susceptibilities are often insensitive to the sign of *D*, and for complex **2** the data could be obtained with either a positive or negative *D* value.[1, 2] Based on previous, reported values the sign of *D* is most likely positive.[3, 4]

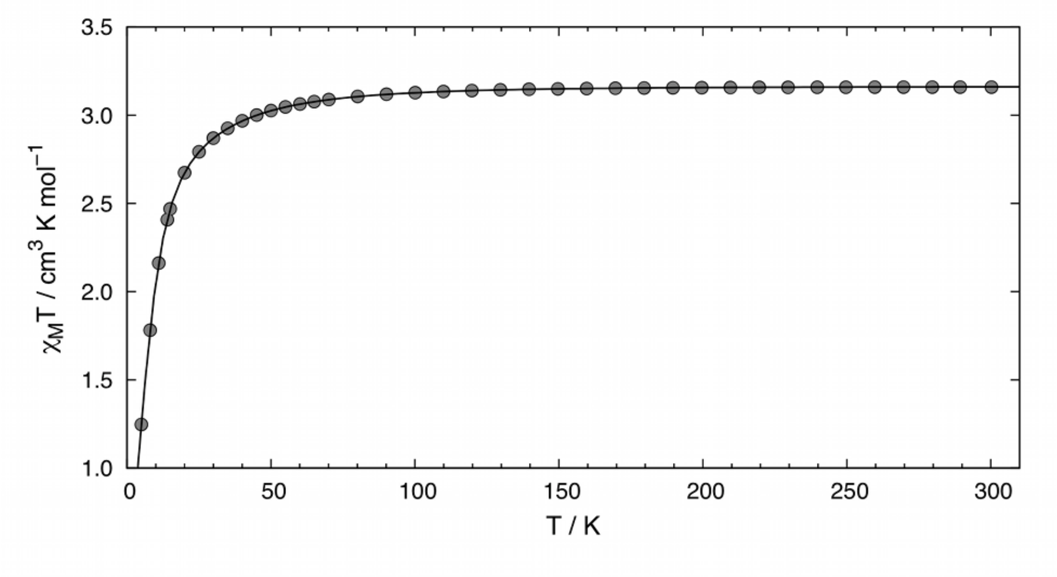

Figure S5. Temperature dependence of χ_MT for **2**, measured at 0.1 T.

SQUID Magnetometry of the red crystals:

Figure S6 depicts the plot of $\chi_M T$ vs T for the red crystals. $\chi_M T$ steadily decreases with decreasing temperature from 3.18 cm^3 mol^{-1} K at 300 K to 1.68 cm^3 mol^{-1} K at 5.0 K. The 300 K value is higher than the expected spin-only (g = 2) value of 3.00 cm^3 mol^{-1} K for a high spin Fe^{II} complex, which can be attributed to the presence of significant spin-orbit coupling effects. It has been previously seen that high spin Fe^{II} square planar complexes possess an appreciable zero-field splitting (ZFS) parameter, D. On the basis of this consideration, the experimental magnetic susceptibility data were fit to the theoretical expression given in eq. S2, which describes the powder average χ_M vs T behavior for a mixture of two compounds with $S = 2$ undergoing zero-field splitting, where $x_i = D_i/kT$, N is Avogadro's number, D_i is the axial single-ion ZFS parameter for compound i, TIP is the temperature-independent paramagnetism, Θ is the Weiss constant, g_i is the average g factor for compound i, and p is the mole fraction of the compound with i = 2.

$$\chi_M T = \{[(1-p)\chi_{M1}] + (p\chi_{M2}) + TIP\}T \qquad \text{(eq. S2)}$$

where
$$\chi_{Mi} = \frac{Ng_i^2\mu_\beta^2}{3k(T-\Theta)}\left[\frac{2e^{-x_i}+8e^{-4x_i}}{1+2e^{-x_i}+2e^{-4x_i}}\right] + \frac{2Ng_i^2\mu_\beta^2}{3k(T-\Theta)}\left[\frac{\frac{6}{x_i}(1-e^{-x_i})+\frac{4}{3x_i}(e^{-x_i}-e^{-4x_i})}{1+2e^{-x_i}+2e^{-4x_i}}\right]$$

The data were fit in the temperature range of 300 K – 15 K, and yielded fit parameters of $|D_1|$ = 7.35(5) cm^{-1}, g_1 = 2.07(2), $|D_2|$ = 17.4(1) cm^{-1}, g_2 = 2.13(4), Θ = -5.44 K, p = 0.1, and no TIP term. The Weiss constant can be determined from a plot of $1/\chi_M$ vs T. The value obtained from this plot was in good agreement with the value obtained from the fit, suggesting the presence of intramolecular exchange interactions. It is important to note that the ratio p changes from one crystallization to the next and for this sample p = 0.1 provides the best fit.

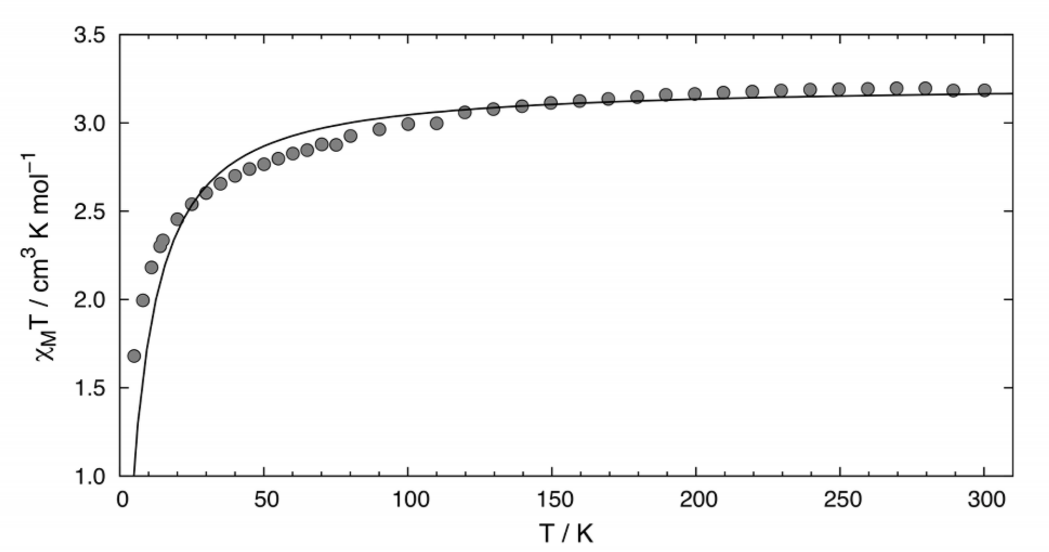

Figure S6. Temperature dependence of χ_MT for the red crystals, measured at 0.1 T. The fit is not as good as that of **2** due the greater distortion of the second conformer seen in the crystal structure, requiring equations based on rhombic rather than axial symmetry, which would suffer from overparameterization of the fit.

5. High-field EPR spectroscopy of 2.

The analysis of the high-field EPR spectra was performed in the framework of a standard S = 2 spin-Hamiltonian, equation S3, using the methodology outlined in references.[5, 6] All symbols of equation S3 have their usual meaning and while the first term accounts for the Zeeman interaction the second takes in consideration the zero-field splitting (ZFS) of the quintet ground state.

$$\widehat{\mathrm{H}}_e = \mu_{\mathrm{B}}\,\mathbf{B}\cdot\tilde{g}\cdot\vec{\mathbf{S}} + D\left[\hat{S}_z^2 - \tfrac{1}{3}S(S+1) + \tfrac{E}{D}\left(\hat{S}_x^2 - \hat{S}_y^2\right)\right] \qquad \text{(eq. S3)}$$

We have investigated a series of eleven samples that included both ground and not ground microcrystalline brown **2** as well as recrystallized **2** as ground red crystals. The purity of each sample was assessed on the basis of the 4.2 K, zero-field Mössbauer spectra recorded for the respective sample. At low temperature, for the 400 GHz frequency range the spectra of **2** as brown microcrystalline powder exhibits a distinct spectrum that is easily recognizable by the presence of two dissimilar resonances, an absorption-shaped resonance centered at ~ 2.0 T and another with a derivative shape occurring at ~ 5.5 T, see Figures 4 and Figure S7. At lower frequencies, in the 200 - 300 GHz range, these spectra exhibit a single resonance that moves to lower fields with increasing frequency. In Figure S8 these features are marked by the (b) symbol. The field and frequency dependence of these three resonances is summarized in Figure 5. Our analysis shows that D > 0, that the two features of the 400 GHz spectra correspond to the *x* and *y* and the resonance observed at lower frequencies corresponds to the *z* component of the g tensor, and that they are ground-state resonances, see Figure S7. For a negative D, at low temperature we expect to observe spectra that exhibit a single resonance which moves to higher fields with increasing frequency. Finally, we found that D = 17.4(1) cm^{-1}, E/D = 0.14(2), g_x = 2.19(1), g_y = 2.18(1) and g_z = 2.04(1).

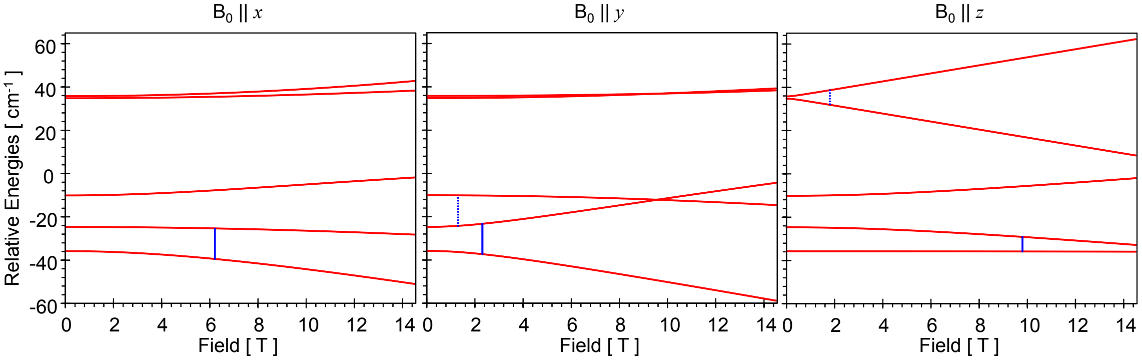

Figure S7. Energy levels of a S = 2 system plotted for D = 17.4 cm^{-1}, E/D = 0.14, g_x = g_y = 2.2 and g_z = 2.0 as function of the applied field aligned with the *x* (*left*), *y* (*middle*) and *z* (*right*) components of the ZFS and g tensors. The vertical blue lines illustrate the position of the allowed resonances for an incident microwave frequency ν = 422 GHz for B$_0$ || *x*, *y* and ν = 203 GHz for B$_0$ || *z*.

Interestingly, under identical experimental conditions the spectra recorded for **2** as ground red crystals exhibit two distinct spectral components. Although, one of these components is essentially identical to that observed for **2** as brown microcrystalline powder, the other cannot be rationalized by considering a D ≈ 17 cm^{-1}. Thus, comparison of the spectra obtained for the red crystals, see Figure S8, with those recorded for the brown powder shows that the former exhibits at least one additional resonance marked by (r). Since the zero-field Mössbauer spectra recorded for **2** as brown microcrystalline powder and for **2** as red crystals display identical quadrupole doublets (see Figure S10, Figure S14, Figure S15), the second spectral component of the latter cannot be associated with a distinct chemical species, i.e. it is not the product of a decay process. Although we have found that the relative ratio of the two spectral components is sample dependent we do not yet understand all the factors that control their relative amounts. Our experiments suggest that protracted mechanical manipulation of **2** as red crystals, e.g. grinding, sample transfer between different containers (see Figure S14), leads to an increased fraction of the D ≈ 17 cm^{-1} spectral component associated with **2** as brown microcrystalline powder. This strong dependence of the intensity of the novel spectral component on the mechanical treatment of the sample, in particular on grinding, renders our efforts to extract its spectroscopic parameters by high-field EPR particularly challenging. These difficulties originate from the fact that single crystals exhibit intense resonances that appear at field positions which are orientation dependent. Our spectral analysis relies on the implicit assumption that we investigate powder samples for which all molecules are randomly distributed, requirement which for crystalline powders can be fulfilled only by thorough grinding.

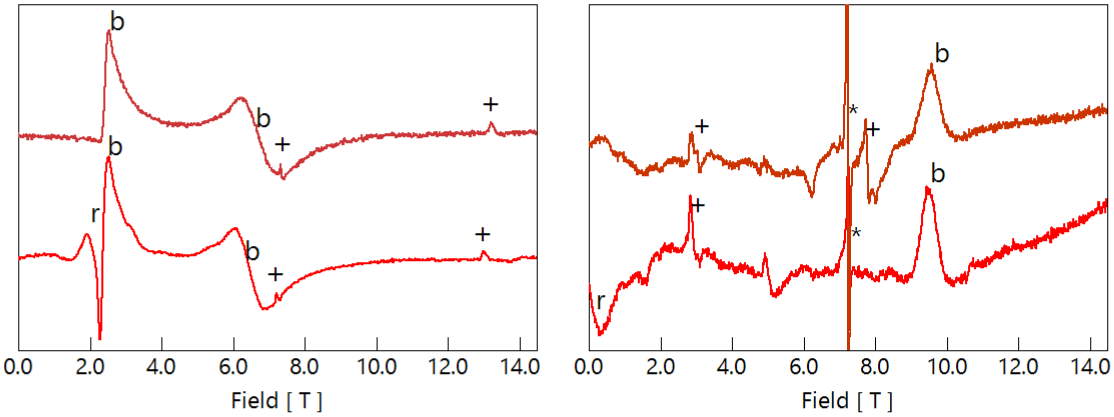

Figure S8. 5 K high-field EPR spectra recorded for **2** as brown microcrystalline powder (*top*) and as ground red crystals (*bottom*). The *left* panel compares spectra recorded in the 400 GHz frequency range respectively, at 429 GHz (*top*) and 422 GHz (*bottom*), the *right* panel exhibits spectra recorded at 203 GHz. The resonances marked by (+) originate from molecular $O_2(g)$ adsorbed on the surface of the plastic containers and those marked by (*) appear at g = 2.003 and is due to a free radical contaminant.

Although we have performed extensive simulations trying to extract the parameters of the second spectral component and have investigated multiple samples we have not been able to obtain a satisfactory solution. Furthermore, due to the grinding-dependent fraction of this component based on the EPR spectra alone we could never rule out that this component does not account for partially oriented single crystals. Still, interrogation of the field and frequency dependency observed for the novel resonance of the ~ 200 GHz spectra suggests a behavior consistent with a $\Delta m = \pm 3$ transition, i.e. $|S = 2, M = -1\rangle \rightarrow |S = 2, M = 2\rangle$ of a S = 2 spin system, and a considerably smaller (D ~ 3 cm^{-1}) and axial (E/D ~ 0) ZFS tensor.

6. Mössbauer spectroscopy of 2.

We have investigated a series of six Mössbauer samples of microcrystalline brown **2** as well as of recrystallized **2** as red crystals. The spectra were analyzed in the framework of a S = 2 Hamiltonian obtained by updating equation S3 with terms that describe ^{57}Fe hyperfine interactions:

$$\hat{\mathrm{H}} = \hat{\mathrm{H}}_e + \hat{\mathrm{H}}_{hf} \tag{eq. S4}$$

where:

$$\hat{\mathrm{H}}_{hf} = \delta + \hat{\mathrm{H}}_Q - g_n \beta_n \vec{\mathbf{B}} \cdot \hat{\mathbf{I}} + \hat{\mathbf{S}} \cdot \tilde{\mathbf{A}} \cdot \hat{\mathbf{I}} \tag{eq. S5a}$$

$$\hat{\mathrm{H}}_Q = \frac{eQV_{ZZ}}{12}\left[3\hat{I}_{\mathrm{Z}}^2 - I(I+1) + \eta(\hat{I}_{\mathrm{X}}^2 - \hat{I}_{\mathrm{Y}}^2)\right] \tag{eq. S5b}$$

$$\eta = \frac{V_{XX} - V_{YY}}{V_{ZZ}} \tag{eq. S5c}$$

$$\Delta \mathrm{E}_Q = \frac{1}{2} eQV_{ZZ}\sqrt{1 + \frac{\eta^2}{3}} \tag{eq. S5d}$$

The terms of equation S5a account for, from left to right: (*i*) the contribution of the isomer shift δ; (*ii*) electric quadrupole interaction; (*iii*) nuclear Zeeman interaction; (*iv*) magnetic hyperfine interaction. Although we have attempted to confine our analysis to solutions for which all tensors were kept collinear we found that the spectra of **2** as red crystals are best represented by our simulations when the electric field gradient (EFG) tensor is rotated from the reference frame (*x*, *y*, *z*) of the ZFS tensor. Equations S5b - d are written such that the EFG tensor is expressed in its standard, principal axis frame (X, Y, Z). The relative orientation of (X, Y, Z) frame with respect to the (*x, y, z*) reference frame is described using a standard set of Euler angles (α, β, γ). Additionally, for the analysis of the spectra recorded for recrystallized **2** as red crystals we have included the magnetic interactions between two near molecular neighbors. For the latter we used a spin Hamiltonian obtained by considering two sites (i = 1, 2), and by amending equation S4 with a term that describes the exchange interaction:

$$\hat{\mathrm{H}} = J\hat{\mathbf{S}}_1 \cdot \hat{\mathbf{S}}_2 + \sum_{i=1}^{2}\left[\hat{\mathrm{H}}_e(i) + \hat{\mathrm{H}}_{hf}(i)\right] \qquad \text{(eq. S6)}$$

The field-induced magnetic hyperfine splitting of the Mössbauer spectra arises from the interaction of ^{57}Fe nuclei with an effective field, $\vec{\mathbf{B}}_{eff} = \vec{\mathbf{B}}_{int} + \vec{\mathbf{B}}$, that results from the vector sum of the applied field, $\vec{\mathbf{B}}$, and the internal field, $\vec{\mathbf{B}}_{int} = -\langle\vec{\hat{\mathbf{S}}}\rangle \cdot \tilde{\mathbf{A}}/g_n\beta_n$. Inspection of the energy diagram of Figure S7 shows that based on the EPR parameters, while B ≤ 8.0 T the $|0\rangle$ ground sublevel of **2** as brown microcrystalline powder is well separated from the first excited magnetic sublevel and thus at 4.2 K essentially only the $|0\rangle$ sublevel is thermally populated. Hence, the thermally averaged spin expectation value is in effect nearly identical to the spin expectation value calculated for the $|0\rangle$ sublevel. Consequently, for D >> 0 the spectra are insensitive to the flip rate of the electronic spin and thus we have conducted all our simulations assuming a fast relaxation rate for the electronic spin, i.e. spin flip rate larger than 10^{-7} s^{-1}. Under these conditions $\langle\vec{\hat{\mathbf{S}}}\rangle = \langle\vec{\hat{\mathbf{S}}}\rangle_{th}$ where $\langle\vec{\hat{\mathbf{S}}}\rangle_{th}$ is obtained through the thermal averaging of $\langle\vec{\hat{\mathbf{S}}}\rangle$ over the entire set of sublevels of the spin multiplet. Figure S9, *red* illustrates both the field– and the temperature–dependence calculated at 4.2 K (*left*) and respectively, in 8 T (*right*) of the thermal spin expectation values of an S = 2 using the ZFS and g tensors values obtained from the analysis of the high-field EPR spectra of **2** as a brown microcrystalline powder. At 4.2 K the increase in the spin expectation value and thus in the internal field arises from the mixing of the $|\mathrm{S} = 2, \mathrm{M} = \pm 1\rangle$ magnetic doublet into the ground $|0\rangle \cong$

$|\mathrm{S}=2,\mathrm{M}=0\rangle$ sublevel (for D = 17.4 cm^{-1} and E/D = 0.14 the ground sublevel of quintet spin system is given by $|0\rangle = 0.9929|2{,}0\rangle - 0.0839(|2{,}2\rangle + |2{,}{-2}\rangle))$ by the x and y components of the applied field and thus, while $\langle\hat{\mathrm{S}}_\mathrm{x}\rangle_{th}$ and $\langle\hat{\mathrm{S}}_\mathrm{y}\rangle_{th}$ exhibit a strong dependence on the applied field $\langle\hat{\mathrm{S}}_\mathrm{z}\rangle_{th} \approx 0$. Therefore, the simulations of field–dependent, 4.2 K spectra of **2** as brown microcrystalline powder are strongly dependent on A_x, A_y and are essentially independent of A_z, component which can only be determined from the analysis of the high–field (B > 6 T), variable–temperature spectra. For $\mu_\mathrm{B}\mathrm{B} \ll \mathrm{D}$ and D >> 0, a D value such as that observed for **2** as brown microcrystalline powder, we found that the $\langle\hat{\mathrm{S}}_{\mathrm{x,y}}\rangle$ spin expectation values of the $|0\rangle$ ground sublevel are well described by equations S7 a-c.

$$\langle\hat{\mathrm{S}}_\mathrm{x}\rangle \cong -\frac{6\mathrm{g_x}\mu_\mathrm{B}\mathrm{B}}{\mathrm{D}+3\mathrm{E}} \qquad \text{(eq. S7a)}$$

$$\langle\hat{\mathrm{S}}_\mathrm{y}\rangle \cong -\frac{6\mathrm{g_y}\mu_\mathrm{B}\mathrm{B}}{\mathrm{D}-3\mathrm{E}} \qquad \text{(eq. S7b)}$$

$$\langle\hat{\mathrm{S}}_\mathrm{z}\rangle \cong 0 \qquad \text{(eq. S7c)}$$

The spectral simulations of Figures 6, Figure S10, Figure S11 of the spectra recorded for **2** as brown microcrystalline powder were obtained using the ZFS and g tensors determined from the analysis of the high-field EPR spectra (D = 17.4 cm^{-1}, E/D = 0.14, g_x = 2.19, g_y = 2.18 and g_z = 2.04). Inspection of Figure S9 (*right*) shows that above 120 K the $\langle\hat{\mathrm{S}}_{\mathrm{x,y,z}}\rangle_{th}$ values are nearly equal and essentially independent of the ZFS. Furthermore, $\langle\hat{\mathrm{S}}\rangle_{th} \sim 1/T$ and the associated $\mathrm{B}_{int,j} \cong \frac{g_j\mu_\mathrm{B}\mathrm{B}}{3\mathrm{kT}} A_j S(S+1)$ where $j = x, y, z$ is small and the spectra are dominated by the nuclear Zeeman and quadrupole interactions. Under these conditions we have assessed the sign of ΔE_Q, the value of η as well as of A_z.

Thus we have found that the spectra of **2** both as brown microcrystalline powder and as red crystals are best described using $\Delta E_Q < 0$ and $\eta = 0.6(2)$. The parameter set that yield our best simulations of the spectra recorded for **2** as brown microcrystalline powder was obtained following a comprehensive analysis of the entire set of spectra and is presented in Table S1.

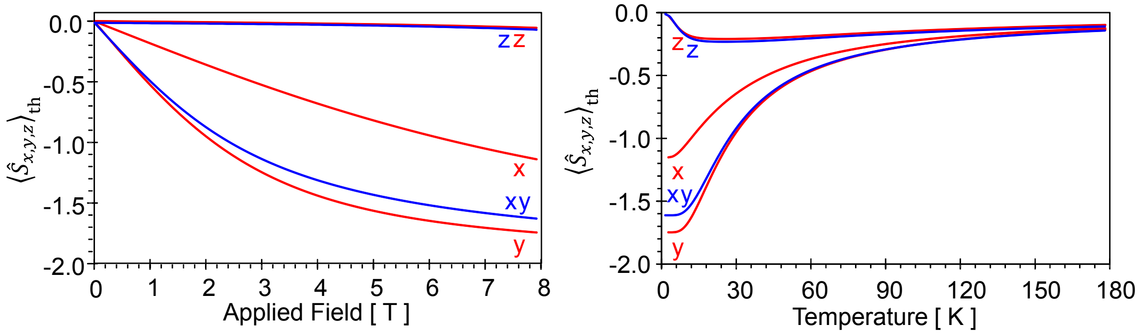

Figure S9. In *red* are shown the thermally averaged spin expectation values $\langle \hat{\mathbf{S}}_{\mathbf{x,y,z}} \rangle_{th}$ obtained for a S = 2 spin system using equation S3 and D = 17.4 cm^{-1}, E/D = 0.14, g_x = 2.2, g_y = 2.2 and g_z = 2.0. In *blue* are shown the thermally averaged spin expectation values $\langle \hat{\mathbf{S}}_{\mathbf{x,y,z}} \rangle_{th}$ obtained for a two-spin system enclosing two S = 2 sites, values predicted using equation S6 with $D_{1,2}$ = 17.4 cm^{-1}, $(E/D)_{1,2}$ = 0.0, $g_{x1,2}$ = 2.2, $g_{y1,2}$ = 2.2, $g_{z1,2}$ = 2.0 and J = -1.6 cm^{-1}. These values were calculated at 4.2 K and plotted as function of the applied field (*left*) and as function of temperature for a 8.0 T applied field (*right*).

Inspection of Figure S10, Figure S11, Figure S13, Figure S14 shows that although at 4.2 K, 0.0 T the spectra of the red and brown forms of **2** consist of quadrupole doublets that are essentially identical they exhibit distinctly different field-dependent behavior. Comparison of these spectra shows that although they reveal a magnetic hyperfine splitting of similar magnitude, the spectra of **2** as red crystals are more symmetric. The asymmetry of the spectra recorded for **2** as a brown microcrystalline powder has been rationalized by the presence of large E term that is, a rhombic ZFS tensor. While the increased symmetry of the spectra of **2** as red crystals can be explained by considering axial ZFS and A tensors, i.e. E ≈ 0 and $A_x \approx A_y \neq A_z$, inspection of equations S7a-c suggests that while E ≈ 0 to attain for **2** as red crystals an internal field equal in magnitude to the largest component of internal field observed for **2** as a brown microcrystalline powder ($B_{int,y}$) either D has to be sizably smaller or the considered g-values have to be dramatically larger.

Table S1. Fine structure and hyperfine structure parameters of **2** derived from the combined analysis of the Mössbauer and high-field EPR spectra of **2** as brown microcrystalline powder and from the analysis of the Mössbauer spectra of **2** as ground red crystals.

Sample	**D** [cm^{-1}]	**E/D**	$g_{x,y,z}$	**J** [cm^{-1}]	**δ** [mm/s]	**ΔE$_Q$** [mm/s]	**η**	$A_{x,y,z}/g_n\beta_n$ [T]
2 brown	$17.4^{a,c}$	0.14^{c}	$2.19, 2.18, 2.04^{c}$	n.a.	0.82(1)	$-0.45(1)^{d}$	$0.6(2)^{d}$	-17(1), -13(1), -30(2)
2 red	*$12(2)^{a}$*	*0.01(1)*	*2.8(1), 2.8(1), 2.1(1)*					*-12.4(4), -12.5(5), -23(3)*
	$16(2)^{b}$	0.01(1)	$2.2, 2.2, 2.0^{e}$	-1.6(4)				-12.5(5), -14.2(2), -29(3)

a) Parameters obtained using equation S4 of describing spin-Hamiltonian of an isolated S = 2 site.
b) Parameters obtained using equation S6 that describes the spin-Hamiltonian of a two, magnetically interacting S = 2 spins. The two local iron sites were kept identical.
c) Values determined from the analysis of the high-field EPR spectra.
d) The electric field gradient tensors (EFG) are rotated relative to the ZFS tensor using α = 0°(0°), β = 90°(45°), γ = 90°(90°) for the **2** as brown powder (red crystals). The (α, β, γ) Euler angles account for the rotation of the (X, Y, Z) frame of the EFG tensor with respect to the (*x, y, z*) frame of the ZFS tensor. For the **2** as brown powder, in the ZFS tensor frame the EFG tensor can also be described using ΔE_Q = 0.45 mm/s and η = -1.6.
e) Fixed values.

Indeed, we could obtain a good representation of the field-dependent 4.2 K, and of the high-temperature (T > 100 K) spectra of **2** as red crystals using D ≈ 8 cm^{-1}, E ≈ 0 and $g_x = g_y = 2.2$, $g_z = 2.0$. However, by using these values we could not account for the observed 20 - 50 K, 8 T spectra - conditions under which the simulations are most sensitive to zero-field splitting. By using equation S4 we obtained a good representation of the entire set of spectra only by allowing for a dramatic increase in the absolute value of the g-tensor components and a D value considerably smaller than the 17.4 cm^{-1} value observed for **2** as a brown powder. Our best simulations obtained using equation S4 are shown in

Figure S10 and Figure S11 and were obtained using the parameter values listed in Table S1 (*italic*).

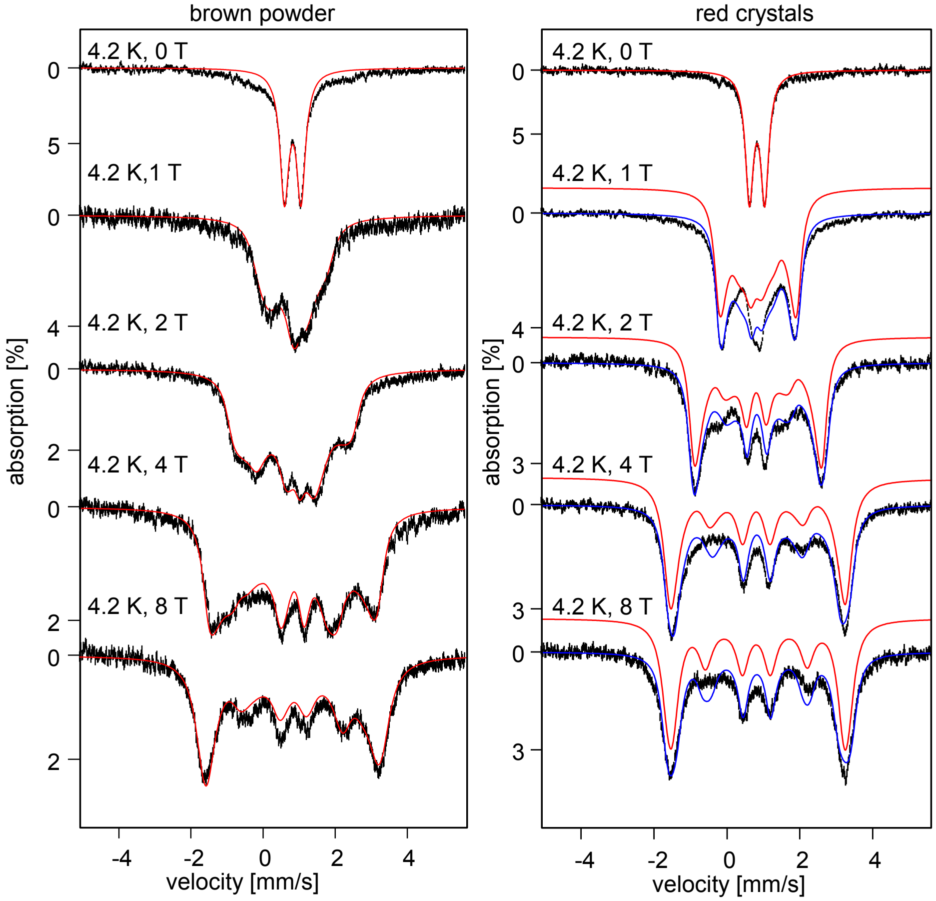

Figure S10. Variable-field Mössbauer spectra recorded at 4.2 K for **2** as brown microcrystalline powder (*left*) and as red crystals (*right*). The solid *red* lines are simulations obtained using equation S4, the solid *blue* lines were obtained using equation S6. The parameters used for these simulations are listed in **Table S1**.

The parameter set obtained from the spectral simulations of **2** as red crystals using equation S4 is rather uncommon. Thus, not only are the g-values unusually large but also simple crystal-field theory based arguments that can be made with respect to the expected spin-orbit coupling interactions responsible for the observed ZFS and g tensors suggest that a decrease in D concomitant with an increase in g values is, if not unlikely, at least rather unusual. Thus, we have searched for solutions that considered ZFS and g tensors similar to those observed for **2** as a brown microcrystalline powder. Consequently, we realized that inclusion of a relatively small exchange interaction between two neighbors has an outsized effect on the simulations of the 20 – 50 K, 8 T spectra as well as of those recorded at 4.2 K for B < 4T and thus its inclusion offers an alternative justification for the observed behavior.

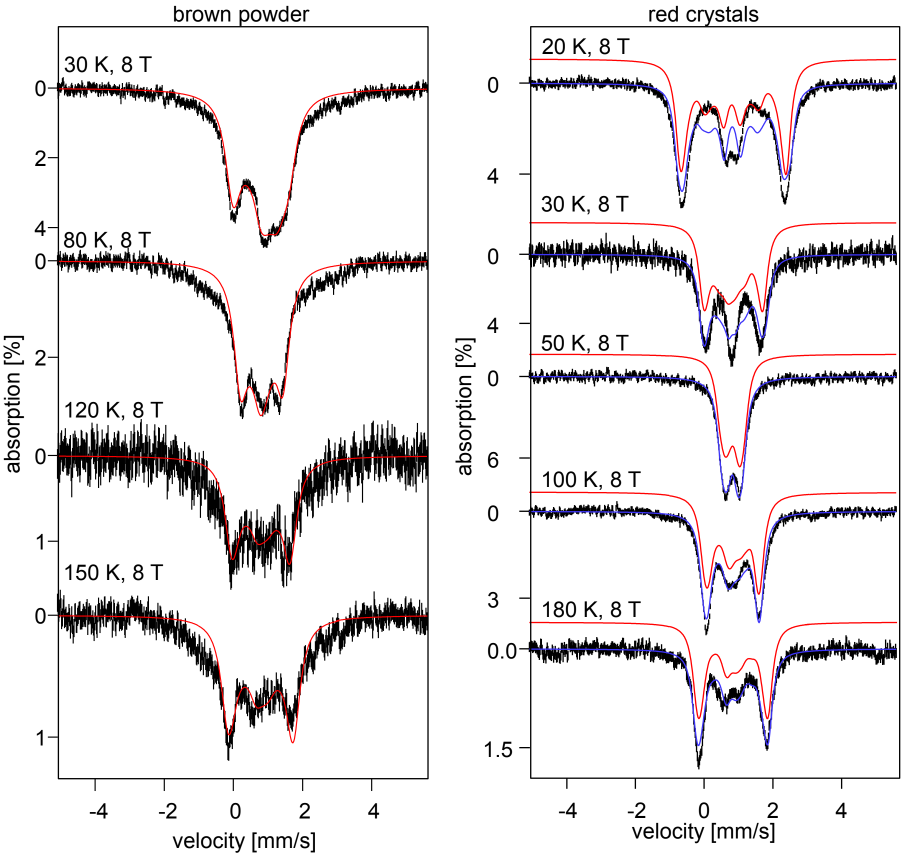

Figure S11. Variable-temperature Mössbauer spectra recorded in a 8 T applied field for **2** as brown microcrystalline powder (*left*) and as red crystals (*right*). The solid *red* lines are simulations obtained using equation S4, the solid *blue* lines were obtained using equation S6 The parameters used for these simulations are listed in **Table S1**.

The origin of this effect can be rationalized by considering equations S8a-b obtained from a perturbation treatment of the Zeeman and exchange interactions in the presence of a large, positive, and axial ZFS tensor (D >> 0, E = 0). Furthermore, Figure S12 illustrates the predicted dependence of the thermal spin expectation values of a local iron sites on the exchange coupling constant J obtained at 4.2 K, 2 T from the full diagonalization of the spin-Hamiltonian matrix obtained using equation S4 (red) and S6 (blue). Thus, in addition to having an axial ZFS tensor (E ~ 0) this analysis suggests that the presence of a relatively small *ferromagnetic* interaction J ≈ 2 cm^{-1} can account for the differences between the red and brown forms of **2**.

$$\langle \hat{S}_{x,y} \rangle \cong -\frac{6 g_{x,y} \mu_B B}{D}\left(1 - \frac{3}{2}\frac{J}{D}\right) \qquad \text{(eq. S8a)}$$

$$\langle \hat{S}_z \rangle \cong 0 \qquad \text{(eq. S8b)}$$

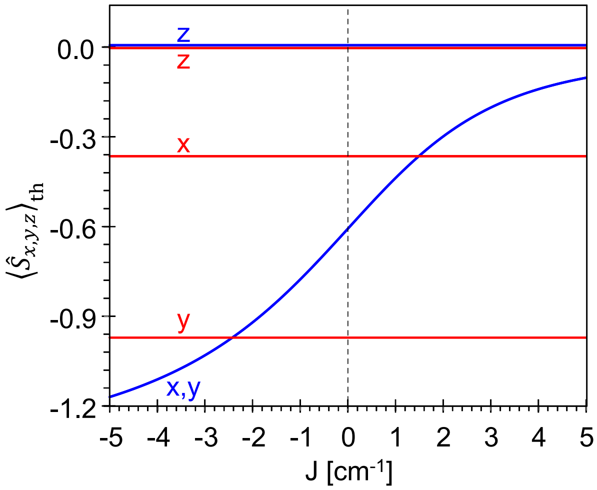

Figure S12. Thermally averaged spin expectation values $\langle \hat{\mathbf{S}}_{\mathbf{x,y,z}} \rangle_{th}$ obtained for a single S = 2 spin system using equation S3 (*red*) with D = 17.4 cm^{-1}, E/D = 0.14, g_x = 2.2, g_y = 2.2, g_z = 2.0 and using equation S6 (*blue*) for two identical, magnetically interacting S = 2 spins for which the local parameters are D = 17.4 cm^{-1}, E/D = 0.00, g_x = 2.2, g_y = 2.2, g_z = 2.0. These values were calculated at 4.2 K, 2.0 T and plotted as function of the exchange coupling J (J < 0 corresponds to a ferromagnetic interaction).

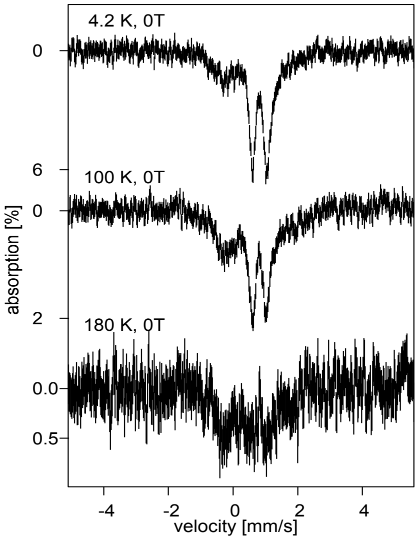

Figure S13. Zero-field, variable-temperature Mössbauer spectra recorded for **2** as a brown microcrystalline powder. In addition to the narrow quadrupole doublet of **2** these spectra also exhibit two broad resonances that account for a ferric decay product (at 4.2 K $\delta = 0.55$ mm/s, $\Delta E_Q = 1.6$ mm/s and ~ 30% of the area). These spectra illustrate the dramatic drop with increasing temperature in the recoilless fraction *f* observed for **2** as a brown powder.

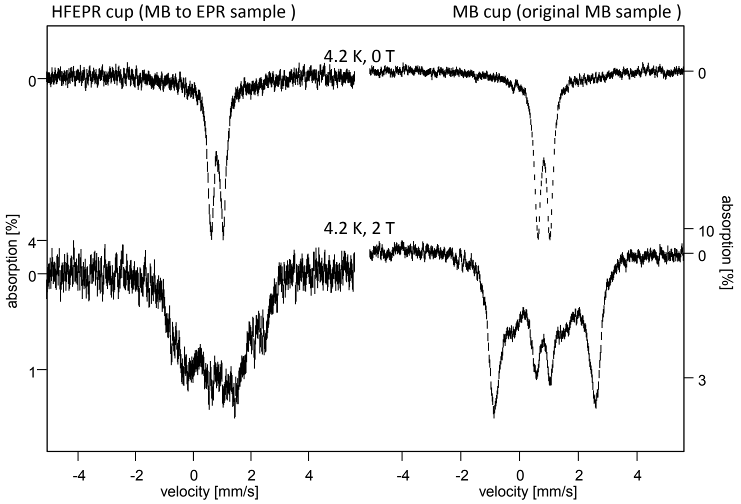

Figure S14. Comparison of the spectra recorded for **2** as a brown microcrystalline powder recorded for the same sample of discussed above, recorded before and after transfer from the original Mössbauer sample holder into an EPR container. The transfer was performed at 77 K by manipulating the powder under liquid nitrogen. The 2 T spectra illustrate the increased sensitivity of **2** as red crystals to mechanical manipulations.

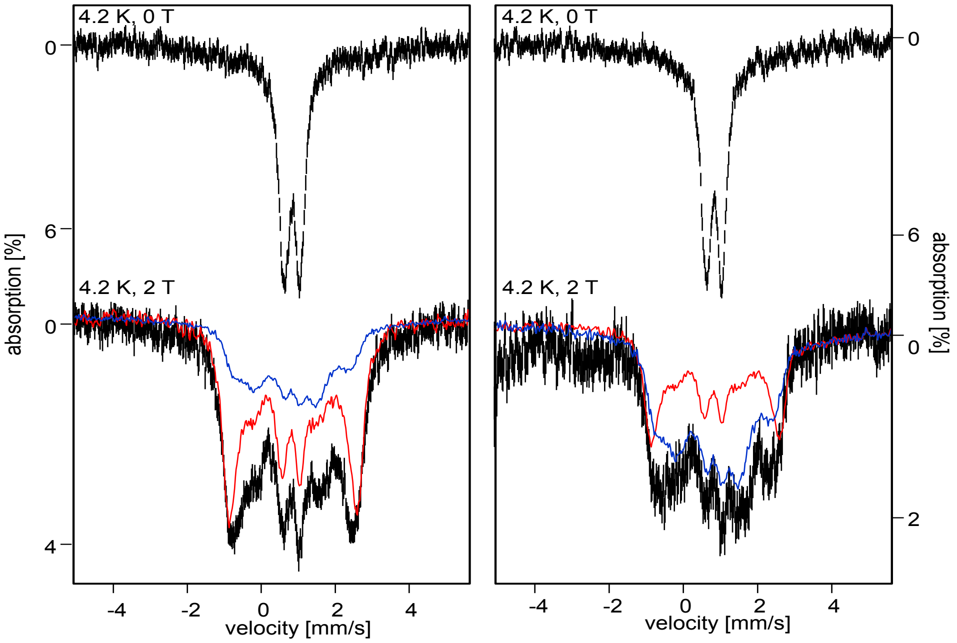

Figure S15. Comparison of spectra recorded for two additional samples of recrystallized **2** as red crystals. Interestingly, these samples exhibit field-dependent spectra that can be deconvoluted into two spectral components. The individual components are constituted by the spectra shown in Figure S10 and Figure S11 obtained for **2** as a brown powder (blue) and as red crystals (red).

With exception of the particular sample for which the spectra are shown in Figure S10, Figure S11, Figure S12, Figure S13, and Figure S14, the variable-field spectra recorded for samples of recrystallized **2** as red crystals exhibit two distinct spectral components. This observation is illustrated in Figure S15 that shows spectra obtained for two additional samples of **2** as red crystals. Thus, the field dependent spectra obtained for these samples can be deconvoluted into a sum of the spectra shown in Figure S10 and Figure S11. Although we have attempted to rationalize the factors responsible for the relative ratio of the two components, we have not been able to find a satisfactory justification of our observations. Since the Mössbauer spectra of Figure S10, Figure S11, Figure S12, Figure S13, and Figure S14 recorded for **2** as red crystals showed that this sample is essentially free of the spectral component associated with **2** as a brown microcrystalline powder we have attempted to study the same material by high-field EPR. Thus we have transferred the contents of this Mössbauer sample into an EPR container at 77 K under liquid nitrogen. To our surprise the EPR spectra recorded for this sample were similar with those shown in Figure S8 suggesting that a large fraction of the sample was converted from **2** as red crystals into the fraction associated with **2** as a brown microcrystalline powder. Indeed, the 2 T, 4.2 K spectrum of Figure S14 recorded for the converted sample shows that the mechanical manipulation of this sample led to its conversion.

The zero-field spectrum recorded at 4.2 K for a ^{57}Fe enriched toluene solution of **2** exhibits two distinct quadrupole doublets (Figure 7). For this sample more than 70 % of the iron can be ascribed to a species which in zero-field exhibits a quadrupole doublet that is essentially identical to that observed for **2** in solid state. The remaining iron amount can be assigned to a high-spin ferrous species that in 0 T displays a broad quadrupole doublet characterized by $\delta = 1.1(1)$ mm/s, $\Delta E_Q = 2.9(1)$ mm/s $\Gamma = 0.6$ mm/s, simulation shown in blue. The solid red lines overlaid over the experimental spectra are simulations obtained using the hyperfine structure parameters determined for **2** as a brown microcrystalline powder and listed in Table S1. Thus, comparison of the 4.2 K, 2 T experimental and theoretical spectra shows that essentially all features observed for the experimental spectrum are well reproduced by the simulated spectrum. Consequently, this observation suggests that dissolving **2** in toluene does not lead to a loss of the square planar geometry and that the electronic structure of the iron site is conserved.

7. DFT calculations

DFT Calculations of 2.

All calculations were performed using Gaussian09.[7] Initial geometries were derived from the X-ray structure with the largest occupation factor (partition **A**). An initial geometry optimization was performed at the unrestricted B3LYP/LANL2DZ level of theory using S = 2 and an effective core potential on the Fe atom, unless otherwise specified. Normal mode analysis was performed on the final geometries, and no negative eigenvalues were found.

Optimized geometry of 2

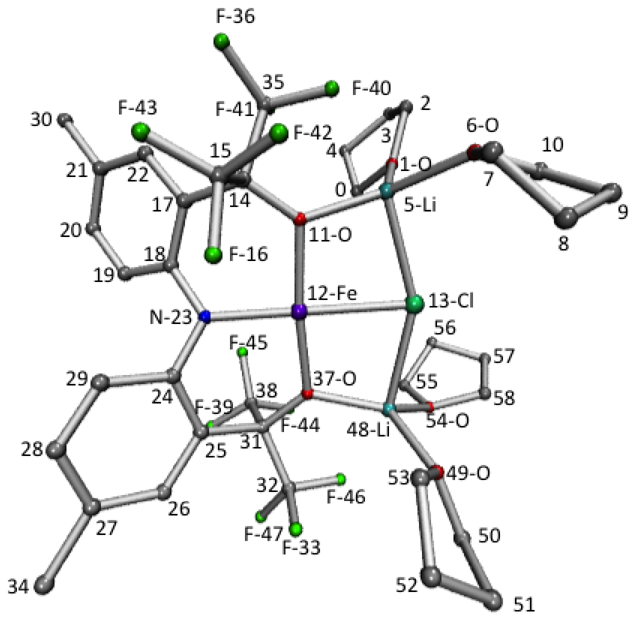

Figure S16. Labeling scheme for the geometry optimization of **2**.

Table S2. Atomic coordinates after geometry optimization of **2**.

Label	Atom	x	y	z
0	C	2.815155	-1.68303	-2.57772
1	O	3.278029	-2.357243	-1.377665
2	C	4.64702	-2.789664	-1.544202
3	C	4.904026	-2.748448	-3.050184
4	C	4.042887	-1.550905	-3.482663
5	Li	2.434988	-1.798856	0.333931
6	O	2.90841	-3.174099	1.686579
7	C	2.641104	-2.882965	3.078209
8	C	1.541355	-3.863325	3.470992
9	C	1.964118	-5.126877	2.70312
10	C	2.564953	-4.556423	1.406749
11	O	1.931455	0.044152	0.394307
12	Fe	-0.000155	0.152961	0.001042
13	Cl	-0.000351	-2.394586	0.002799
14	C	2.732236	1.131863	0.714302
15	C	2.56619	1.449779	2.239311
16	F	1.270925	1.605926	2.564873
17	C	2.463889	2.416032	-0.108238
18	C	1.13506	2.855491	-0.389904
19	C	1.002721	4.043911	-1.157231
20	C	2.088207	4.791318	-1.572997
21	C	3.395088	4.397582	-1.250573
22	C	3.543048	3.218017	-0.525294
23	N	-0.000102	2.155522	0.000663
24	C	-1.135519	2.855298	0.390923
25	C	-2.464173	2.415686	0.108717
26	C	-3.543595	3.217407	0.525617
27	C	-3.396036	4.39684	1.251192
28	C	-2.089318	4.790771	1.574042
29	C	-1.003586	4.043618	1.158458
30	C	4.590956	5.215909	-1.676674
31	C	-2.732014	1.131662	-0.714241
32	C	-4.194454	0.60554	-0.508162
33	F	-4.512194	0.523468	0.800291
34	C	-4.592189	5.214726	1.67734
35	C	4.194592	0.605847	0.507334
36	F	5.149698	1.330608	1.121052
37	O	-1.93134	0.043907	-0.394053
38	C	-2.565182	1.449909	-2.239096
39	F	-3.220825	2.565442	-2.603908
40	F	4.320073	-0.665256	0.993106

41	F	4.511649	0.524116	-0.801309
42	F	3.039654	0.441561	3.023102
43	F	3.22182	2.565355	2.604006
44	F	-3.03806	0.44176	-3.023339
45	F	-1.269786	1.606343	-2.563938
46	F	-4.319641	-0.66545	-0.994318
47	F	-5.149256	1.330422	-1.122202
48	Li	-2.435142	-1.799041	-0.33374
49	O	-3.280104	-2.358357	1.376544
50	C	-4.649378	-2.790392	1.541738
51	C	-4.907542	-2.750122	3.047556
52	C	-4.046164	-1.553301	3.481553
53	C	-2.817757	-1.685494	2.577554
54	O	-2.906274	-3.173744	-1.687491
55	C	-2.638462	-2.882124	-3.078889
56	C	-1.537861	-3.861681	-3.471304
57	C	-1.960206	-5.125725	-2.703986
58	C	-2.562673	-4.55609	-1.407977

Optimized geometry of 2 after removal of THF molecules.

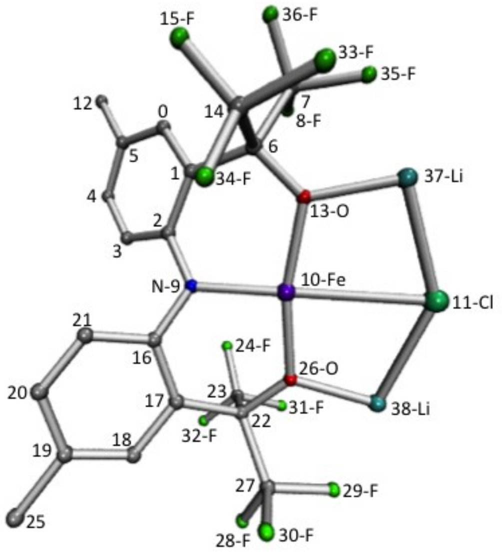

Figure S17. Labeling scheme for the geometry optimization of **2** after removal of THF molecules.

Table S3. Atomic coordinates after geometry optimization of **2** after removal of THF molecules.

Label	Atom	x	y	z
0	C	3.53226	1.706758	-0.829448
1	C	2.465744	0.916765	-0.361045
2	C	1.127343	1.42469	-0.465224
3	C	0.981761	2.660671	-1.14994
4	C	2.05359	3.393742	-1.62394
5	C	3.369111	2.939299	-1.454444
6	C	2.82389	-0.433326	0.303107
7	C	4.108462	-1.091594	-0.319309
8	F	4.084654	-1.071044	-1.652565
9	N	0.000068	0.749356	-0.000666
10	Fe	-0.000064	-1.225935	-0.000892
11	Cl	-0.000139	-3.981543	-0.000137
12	C	4.550731	3.74442	-1.939047
13	O	1.882158	-1.44042	0.159175
14	C	3.052999	-0.23983	1.83207
15	F	4.001893	0.666965	2.107345
16	C	-1.126896	1.424636	0.464664

17	C	-2.465417	0.916833	0.36101
18	C	-3.531621	1.706738	0.830237
19	C	-3.368081	2.939145	1.455425
20	C	-2.052433	3.393242	1.624733
21	C	-0.980886	2.660247	1.14996
22	C	-2.824037	-0.433147	-0.303138
23	C	-3.053891	-0.239378	-1.831958
24	F	-1.91419	0.149458	-2.425796
25	C	-4.549526	3.745515	1.938376
26	O	-1.882381	-1.44043	-0.159805
27	C	-4.108426	-1.091289	0.319811
28	F	-5.278739	-0.600929	-0.103501
29	F	-4.139178	-2.449915	-0.021891
30	F	-4.084047	-1.070788	1.653064
31	F	-3.427385	-1.411005	-2.41815
32	F	-4.002817	0.667595	-2.106564
33	F	3.426077	-1.411655	2.418212
34	F	1.913058	0.148991	2.425427
35	F	4.138872	-2.450214	0.022415
36	F	5.278662	-0.601398	0.104522
37	Li	2.229836	-3.200992	0.247173
38	Li	-2.230257	-3.200997	-0.24645

Optimized geometry of 2 after removal of Li^+ counterions and THF.

The optimized geometry of III is distorted tetrahedral. Using TZVP instead of LANL2DZ results in the same type of geometry.

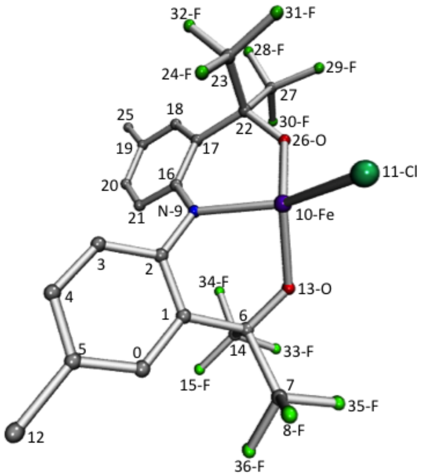

Figure S18. Labeling scheme for the geometry optimization of **2** after removal of Li^+ counterions and THF.

Table S4. Atomic coordinates after geometry optimization of **2** after removal of Li^+ counterions and THF.

Label	Atom	x	y	z
0	C	-0.120256	-0.017949	0.015254
1	C	0.011474	0.026451	1.412726
2	C	1.325265	0.061223	1.975445
3	C	2.41599	0.086036	1.063607
4	C	2.2469	0.058374	-0.309475
5	C	0.961303	0.003062	-0.866834
6	C	-1.246212	-0.038965	2.334948
7	C	-2.532269	0.491924	1.597659
8	F	-2.316791	1.699257	1.041516
9	N	1.562912	0.162269	3.337641
10	Fe	0.330586	1.588344	4.283758
11	Cl	-0.037053	3.951597	4.021968
12	C	0.750562	-0.007943	-2.363519
13	O	-1.192035	0.666195	3.488015
14	C	-1.496675	-1.54882	2.676177
15	F	-1.582518	-2.346553	1.57163
16	C	2.45155	-0.665458	3.95976
17	C	3.0134	-0.405717	5.262407
18	C	3.97209	-1.290208	5.773043
19	C	4.382874	-2.466972	5.139521
20	C	3.766282	-2.766872	3.91767
21	C	2.838105	-1.908058	3.359352
22	C	2.611059	0.852235	6.087883
23	C	3.629206	1.996016	5.750868
24	F	3.510564	2.376616	4.466469
25	C	5.440215	-3.361343	5.742523
26	O	1.342821	1.290864	5.914921
27	C	2.707653	0.584608	7.638048
28	F	3.981681	0.471101	8.14424
29	F	2.144655	1.58113	8.346697
30	F	2.064345	-0.551873	7.980152
31	F	3.444374	3.097714	6.515705
32	F	4.934045	1.631127	5.928135
33	F	-2.652718	-1.735008	3.361399
34	F	-0.507244	-2.049243	3.433708
35	F	-3.566205	0.625937	2.447993
36	F	-3.004858	-0.318418	0.589211

Simulated Mössbauer parameters

All calculations were performed using Gaussian09.[7] The initial geometry was derived from the X-ray structure with the largest occupation factor (partition **A**). An initial geometry optimization was performed at the unrestricted B3LYP/6-311G level of theory using S = 2. The ground state character of the electronic configuration was assessed on the basis of time-dependent (TD) DFT calculations. The default guess led to a state exhibiting one negative excitation and thus, to obtain the proper ground state we performed the appropriate alteration using the *alter* option of the *guess* keyword. Subsequent TD-DFT calculations confirmed the ground state character of this new configuration by yielding only positive excitations. The electric field gradient (EFG) parameters ΔE_Q and η were calculated using the *efg* option of the *prop* Gaussian 09 keyword. The ligand contribution to the EFG tensor was estimated by performing single point calculation in which the high-spin ferrous ion was replaced with a Zn^{2+} ion that has a d^{10} electronic configuration and thus, is expected to have a null valence contribution to the EFG tensor. The predicted isomer shift values were determined from the charge density at the ^{57}Fe nuclei using the calibration of Vrajmasu et al.[8] and single point calculations. The relative energies listed in Table S5 and contour plots of the β-molecular orbitals shown here were obtained using the procedure described in reference six.[9]

Table S5. Summary of the energies and assignments of the four lowest TD-DFT transitions. The molecular frame considered here is such that the z axis is orthogonal to the molecular plane, x is found along Fe-Cl bond, and y is found along the OFeO axis. The *xy* orbital is found out of the plane of the ligand suggesting a sizable mixing with the *xz* orbital.

Transition	**Energy** [cm^{-1}]	**Assignment**	$\langle \hat{S}^2 \rangle$
1	3798	$z^2 \rightarrow \sim xy$	6.003
2	5617	$z^2 \rightarrow \sim xz$	6.003
3	6286	$z^2 \rightarrow yz$	6.003
4	17851	$z^2 \rightarrow x^2\text{-}y^2$	6.007

Table S6. Gross orbital populations of the d-orbital set in the frame of the EFG tensor.

Orbital	**Total**	**Alpha**	**Beta**	**Spin**
z^2	1.839	0.949	0.889	0.059
xz	1.038	0.992	0.045	0.947
yz	1.035	0.996	0.039	0.957
x^2-y^2	1.169	1.001	0.167	0.833
xy	1.045	0.988	0.056	0.931

Table S7. Predicted isomer shift, quadrupole splitting and asymmetry parameter of the EFG tensor.

Parameter	**δ** [mm/s]	**ΔE$_Q$** [mm/s]	**η**
Calculated	0.669	-0.547	0.459
Experimental	0.82(1)	-0.45(1)	0.6(2)

Table S8. EFG tensor components [mm/s]. According to reference [10], four point charges q at distance r along the x, y axes generate a "ligand" EFG tensor that is axial with $\boldsymbol{V_{zz} = -4\frac{q}{r^3}}$ and $\boldsymbol{V_{xx} = V_{yy} = 2\frac{q}{r^3}}$ and since $\boldsymbol{q = -e}$ then $V_{zz} > 0$. Furthermore, a single electron in a pure dz^2 orbital yields "valence" EFG tensor which is also axial with $\boldsymbol{V_{xx} = V_{yy} = \frac{2}{7}\frac{e}{\langle r^3 \rangle}}$ and $\boldsymbol{V_{zz} = -\frac{4}{7}\frac{e}{\langle r^3 \rangle}}$. Therefore, these observations suggest that for a square planar complex supported by ligands that have biting atoms with increased negative charges, we might encounter a situation where the valence contribution is essentially quenched by the ligand contribution to the EFG tensor.

EFG	***xx***	***yy***	***zz***	***xy***	***xz***	***yz***	**principal components**			**ΔE$_Q$**	**η**
Valence	1.632	1.965	-3.598	0.066	-0.009	-0.044	-2.691	1.620	1.072	-2.709	0.203
Ligand	-1.481	-1.593	3.074	-0.023	0.021	0.113	3.077	-1.476	-1.601	3.078	0.040
Total	**0.151**	**0.372**	**-0.523**	**0.043**	**0.012**	**0.069**	**0.385**	**0.143**	**-0.528**	**-0.547**	**0.459**

8. References

1. R. L. Carlin, *Magnetochemistry*, Springer-Verlag, Berlin ; New York, 1986.
2. C. C. Stoumpos, T. C. Stamatatos, H. Sartzi, O. Roubeau, A. J. Tasiopoulos, J. Nastopoulos, S. J. Teat, G. Christou and S. P. Perlepes, *Dalton Trans.*, 2009, 1004.
3. D. Pinkert, S. Demeshko, F. Schax, B. Braun, F. Meyer and C. Limberg, *Angew. Chem. Int. Ed.*, 2013, **52**, 5155-5158.
4. S. A. Cantalupo, S. R. Fiedler, M. P. Shores, A. L. Rheingold and L. H. Doerrer, *Angew. Chem. Int. Ed.*, 2012, **51**, 1000-1005.
5. J. Krzystek, D. Smirnov, C. Schlegel, J. van Slageren, J. Telser and A. Ozarowski, *J. Mag. Res.*, 2011, **213**, 158-165.
6. J. Telser, J. van Slageren, S. Vongtragool, M. Dressel, W. M. Reiff, S. A. Zvyagin, A. Ozarowski and J. Krzystek, *Mag. Res. Chem.*, 2005, **43**, S130-S139.
7. M. J. Frisch, G. W. Trucks, H. B. Schlegel, G. E. Scuseria, M. A. Robb, J. R. Cheeseman, G. Scalmani, V. Barone, B. Mennucci, G. A. Petersson, H. Nakatsuji, M. Caricato, X. Li, H. P. Hratchian, A. F. Izmaylov, J. Bloino, G. Zheng, J. L. Sonnenberg, M. Hada, M. Ehara, K. Toyota, R. Fukuda, J. Hasegawa, M. Ishida, T. Nakajima, Y. Honda, O. Kitao, H. Nakai, T. Vreven, J. Montgomery, J. A., J. E. Peralta, F. Ogliaro, M. Bearpark, J. J. Heyd, E. Brothers, K. N. Kudin, V. N. Staroverov, R. Kobayashi, J. Normand, K. Raghavachari, A. Rendell, J. C. Burant, S. S. Iyengar, J. Tomasi, M. Cossi, N. Rega, J. M. Millam, M. Klene, J. E. Knox, J. B. Cross, V. Bakken, C. Adamo, J. Jaramillo, R. Gomperts, R. E. Stratmann, O. Yazyev, A. J. Austin, R. Cammi, C. Pomelli, J. W. Ochterski, R. L. Martin, K. Morokuma, V. G. Zakrzewski, G. A. Voth, P. Salvador, J. J. Dannenberg, S. Dapprich, A. D. Daniels, Ö. Farkas, J. B. Foresman, J. V. Ortiz, J. Cioslowski and D. J. Fox, Gaussian, Inc., Wallingford CT, Editon edn., 2009.
8. V. Vrajmasu, E. Münck and E. L. Bominaar, *Inorg. Chem.*, 2003, **42**, 5974-5988.
9. S. A. Stoian, Y. Yu, J. M. Smith, P. L. Holland, E. L. Bominaar and E. Münck, *Inorg. Chem.*, 2005, **44**, 4915-4922.
10. P. Gütlich, E. Bill and A. Trautwein, *Mössbauer spectroscopy and transition metal chemistry : fundamentals and application*, Springer, Berlin ; Heidelberg ;, 2011.